Fe-XANES analyses of Reykjanes Ridge basalts: Implications for oceanic crust's role in the solid Earth oxygen cycle

Oliver Shorttle[a], Yves Moussallam[a], Margaret Hartley[a], John Maclennan[a], Marie Edmonds[a], Bramley Murton[b]

[a] *Department of Earth Sciences, University of Cambridge, Downing Street, Cambridge CB2 3EQ, UK*
[b] *National Oceanography Centre, University of Southampton Waterfront Campus, European Way, Southampton, SO14 3ZH, UK*

Abstract

The cycling of material from Earth's surface environment into its interior can couple mantle oxidation state to the evolution of the oceans and atmosphere. A major uncertainty in this exchange is whether altered oceanic crust entering subduction zones can carry the oxidised signal it inherits during alteration at the ridge axis, past the arc front and into the deep mantle for long-term storage. However, recycled oceanic crust may eventually be entrained into mantle upwellings and undergo melting at ocean islands, creating the potential for basalt chemistry to constrain the nature of past solid Earth–hydrosphere redox coupling.

Numerous independent observations suggest that Iceland contains a significant recycled oceanic crustal component, making it an ideal locality to investigate links between redox proxies and geochemical indices of enrichment. We have interrogated the elemental, isotope and redox geochemistry of basalts from the Reykjanes Ridge, which forms a 700 km transect of the Iceland plume. Over this distance, geophysical and geochemical tracers of plume influence increase dramatically, with the basalts recording both long- and short-wavelength heterogeneity in the Iceland plume. We present new high-precision Fe-XANES measurements of $Fe^{3+}/\sum Fe$ on a suite of 64 basalt glasses from the Reykjanes Ridge. These basalts exhibit positive correlations between $Fe^{3+}/\sum Fe$ and trace element and isotopic signals of enrichment, and become progressively oxidised towards Iceland: fractionation-corrected $Fe^{3+}/\sum Fe$ increases by ~ 0.015 and ΔQFM by ~ 0.2 log units. We carefully rule out a role for sulfur degassing in creating this trend, and by considering various redox melting processes and metasomatic source enrichment mechanisms, conclude that an intrinsically oxidised component within the Icelandic mantle is required. Given the previous evidence for entrained oceanic crustal material within the Iceland plume, we consider this the most plausible carrier of the oxidised signal.

To determine the ferric iron content of the recycled component ($[Fe_2O_3]_{source}$) we project observed liquid compositions to an estimate of Fe_2O_3 in the pure enriched endmember melt, and then apply simple fractional melting models, considering lherzolitic and pyroxenitic source mineralogies, to estimate $[Fe_2O_3]_{(source)}$ content. Propagating uncertainty through these steps, we obtain a range of $[Fe_2O_3]_{(source)}$ for the enriched melts (0.9–1.4 wt%) that is significantly greater than the ferric iron content of typical upper mantle lherzo-

lites. This range of ferric iron contents is consistent with a hybridised lherzolite–basalt (pyroxenite) mantle component. The oxidised signal in enriched Icelandic basalts is therefore potential evidence for seafloor–hydrosphere interaction having oxidised ancient mid-ocean ridge crust, generating a return flux of oxygen into the deep mantle.

Keywords: Mantle fO_2, XANES, oxygen, mantle heterogeneity, pyroxenite

1. Introduction

The movement of oxygen between the surface and subsurface of the planet has played a key role in the compositional and physical evolution of all terrestrial reservoirs (Frost, 1991). One means of reconstructing past oxygen fluxes is from mantle rocks, which can preserve chemical signals of ancient and modern redox processes through subduction recycling. Models of the modern surface oxygen budget emphasise the role of oceanic crust as a long-term sink for oxygen via seawater sulfate reduction during hydrothermal processes at the ridge axis (Lécuyer and Ricard, 1999; Sleep, 2005). This oxygen is bound into the oceanic crust as ferric iron (Fe_2O_3) and returned to the mantle during subduction, where it may enter into the mantle's convective circulation, or be rapidly extracted at subduction zones (Kelley and Cottrell, 2009). If subduction has transported oxygen from the hydrosphere into the deep Earth then basalts sampling trace element-enriched mantle domains, which are commonly attributed to ancient recycled oceanic crust (Chase, 1981; Stracke, 2012), should be oxidised relative to basalts sampling ambient mantle (Carmichael, 1991; Lécuyer and Ricard, 1999). However, a prediction that all enriched mantle domains sample oxidised slabs is inconsistent with the recent finding that some enriched mantle domains, far from plumes, are more reduced than ambient mantle (Cottrell and Kelley, 2013). Here we investigate the role of enriched mantle domains in solid Earth redox cycling, with a focused regional study of the Fe_2O_3 content of plume-influenced mid-ocean ridge basalts around Iceland.

We have made new high-precision determinations of the proportion of ferric iron, expressed as $Fe^{3+}/\sum Fe$, by X-ray absorption near edge structure (XANES) spectroscopy in 64 basalt glasses from the Mid-Atlantic Ridge south of Iceland (the Reykjanes Ridge, Murton (1995); Murton et al. (2002)). The compositional variability in these samples offers the potential to probe the oxidation state of enriched and depleted mantle domains on the broad scale of the Iceland swell and geochemical anomaly (Schilling, 1973), as well as the short lengthscale of single enriched seamounts. We begin with a description of the XANES methods we have used to obtain our new dataset. In particular we show that detailed time-resolved observations of the pre-edge structure can rule out beam damage oxidising the iron in natural basalt samples. We then discuss these observations in the context of degassing, crystallisation and melting processes. We remove the effect of

Email address: os258@cam.ac.uk (Oliver Shorttle) (Bramley Murton)

crystallisation and rule out degassing as a significant control on the oxidation state of most Reykjanes Ridge basalts. Finally, we relate the ferric iron data to a model of oceanic crustal recycling and the reintroduction of oxidised material to the mantle.

2. XANES Methods

2.1. Spectral acquisition

Samples were analysed on the I18 beamline at Diamond Light Source (DLS) to probe the detailed pre-edge structure of the Fe K-edge with synchrotron X-rays over the energy range 7020–7500 eV. The X-ray beam was monochromatised using a double Si(333) crystal. The energy step sizes and dwell times used are given in Table A.1. The beam dimensions were 5x3 μm^2, and the experimental geometry had the sample at 45° to the incident X-ray beam and 45° from the collector, giving an incident–fluoresced X-ray angle of 90°. Incident X-ray intensity was measured using a 1.5 cm long ionisation chamber, and the intensity of fluoresced X-rays were measured using a four element silicon drift detector.

Almost all analyses were performed during a single four-day analytical session in August 2014. Sample 98D3, and repeat analyses of 183D2 and 174D9, were performed one month later in a separate session. During our main analytical session the storage ring was operating at 3 GeV with an electron current of 300 mA. For the second session, operating conditions at the beamline had changed: the electron current was now 200 mA and we used a germanium detector with nine elements. In all analyses, attenuation of the primary X-ray beam by 0.1 mm Al plates was employed to keep the count rate below the saturation limit of the detector. These analytical conditions translate into a photon flux of $\sim 10^9$ photons/second.

2.2. Beam damage

Beam damage has been reported during sulfur XANES analyses, where the effect has been to oxidise sulfur in the samples on the timescale of minutes (Wilke et al., 2008; Métrich et al., 2009; Moussallam et al., 2014). A systematic investigation of whether the long-term exposure of basaltic samples to a μ–XANES X-ray beam can cause Fe oxidation/reduction was carried out by Cottrell and Kelley (2009) at NSLS, USA. The Cottrell and Kelley (2009) study found no spectral shift resulting from repeated and extended sample exposure to the X-ray beam (using cumulative exposure times at least twice as great as our 30-minute analyses). At DLS, Moussallam et al. (2014) acquired multiple XANES spectra on the same spot to test whether there was a progressive beam damage effect for Fe, but saw no change in Fe oxidation state despite significant changes in S oxidation. These results imply that Fe is more stable than S during XANES analysis of silicate glasses.

To establish whether beam damage was occurring we performed an additional test using the natural basalt 153D3 from our sample set (0.17 wt% H_2O, typical of Reykjanes Ridge basalts (Nichols et al., 2002)).

The test consisted of positioning the monochromator at a fixed energy of 7114.3 eV, corresponding to the oxidised peak of the pre-edge doublet. Before allowing the beam to illuminate the sample we began collecting the fluoresced X-rays in 1 s time windows, then opened the shutter on the sample. The hypothesis is that if beam damage is occurring we should see a large drift in the fluoresced X-ray count towards higher count rates if the beam damage was oxidative, or towards lower values if the damage was reductive. Instead, with the same analytical conditions as for our measurements we found that no drift in energy occurs at the onset, or thereafter, of the sample being exposed to the beam (Fig. 1A and B). This result indicates that Fe in our samples was neither oxidised nor reduced during the XANES analyses.

We did find that changing the analytical conditions by removing the Al attenuators was able to generate a very small amount of photo-oxidation over the first 700 s of exposure of the sample to the beam (Fig. 1C). However, even this amount of photo-oxidation is over two orders of magnitude less than the natural variability the samples exhibit, and is barely above the instrument stability. Furthermore, that we can see slight photo oxidation under the particular circumstances where the beam is not attenuated, gives us confidence that no photo-oxidation is occurring when we don't see this signal using an attenuated beam.

2.3. Processing of spectra

As has been noted previously (Berry et al., 2003; Farges et al., 2004; Cottrell and Kelley, 2009) the handling of the raw XANES spectra can have a significant influence on the $Fe^{3+}/\sum Fe$ calculated for the unknown materials, which although less significant for a relative study, has the potential to systematically offset the results produced by different groups. To mitigate against this problem we provide a detailed description of the calibration procedure we have selected and include in the supplementary material the normalised spectra we collected so that future comparisons between datasets can be carried out in a self-consistent manner.

The first derivative peak on an Fe foil, 7112.0 eV, measured at the start of the analytical session, provided the energy calibration for the spectra. Following the method of Wilke et al. (2001) a Victoreen function

$$v_1 F^3 + v_2 F^4, \tag{1}$$

was fit to the region 7020–7090 eV before the pre-edge, where $F = I_f/I_0$ is the ratio of fluoresced to incident X-rays and v_1 and v_2 are the parameters to be optimised. The Levenberg-Marquardt optimisation algorithm (Press et al., 1992) was used to find the best fitting parameters. The Victoreen function was subtracted from the spectra, which was then normalised to an edge-step of 1 by taking the average intensity over the region 7250–7400 eV. This energy range was chosen in order to avoid incorporating the highest amplitude oscillation of the post-edge spectrum, which itself moves as a function of $Fe^{3+}/\sum Fe$ (see for example Fig. 2B), potentially making the normalisation sensitive to the sample's oxidation state.

The results of this normalisation routine can be seen in Fig. 2, in which the normalised spectra for samples and reference glasses are plotted.

2.4. Calibration of spectra for $Fe^{3+}/\sum Fe$

We used the NMNH 117393 basalt reference block made by Cottrell and Kelley (2009), and loaned by the Smithsonian Institution National Museum of Natural History, to calibrate $Fe^{3+}/\sum Fe$ in the unknown sample spectra.

A common method for determining the $Fe^{3+}/\sum Fe$ ratio of a material is to use the energy of the $1s \rightarrow 3d$ pre-edge transition, which forms an absorption multiplet prior to the main Fe K-edge (Fig. 2C). The $1s \rightarrow 3d$ pre-edge feature shifts to higher energy and the relative height of its peak changes as $Fe^{3+}/\sum Fe$ increases (e.g. Wong et al. (1984); Bajt et al. (1994) and Fig. 2D), meaning that it can be used to calibrate for $Fe^{3+}/\sum Fe$ in unknowns. A majority of techniques for quantifying the pre-edge feature are 'function fitting' methods, in which a combination of functions are fit to some range of the pre-edge region (between 7100–7120 eV) in order to extract a single parameter (such as centroid energy or peak height ratio) that can be related to $Fe^{3+}/\sum Fe$ (Berry et al., 2003). Often these routines combine two families of functions; one set designed to remove the 'background' associated with the main absorption edge, whilst the second set fits the smaller amplitude pre-edge feature.

However, it is apparent from Fig. 2D that it is not only the $1s \rightarrow 3d$ pre-edge feature that responds to increasing $Fe^{3+}/\sum Fe$ in the glass. The rise to the main absorption edge also moves to higher energy, by up to ~ 1 eV for the range of oxidation states represented in the NMNH 117393 glasses. This is valuable extra information that could potentially be incorporated into forming a calibration for $Fe^{3+}/\sum Fe$ (Berry et al., 2003). Using information beyond simply the position of the $1s \rightarrow 3d$ multiplet would be especially useful for natural mid-ocean ridge basalt (MORB) samples, in which the absolute variability of $Fe^{3+}/\sum Fe$ so far reported by XANES is extremely limited ($\sim 3\%$ (Cottrell and Kelley, 2011, 2013)).

In order to maximise the amount of information we use in calibrating the unknown spectra for $Fe^{3+}/\sum Fe$, and thereby increase the signal to noise, we have used principal component regression (PCR). PCR is a linear mixing method (e.g. Manceau et al. (1992); Farges et al. (2004)) which first identifies spectral features corresponding to the maximum variance in the dataset through conventional principal component analysis (PCA). For the reference spectra with known $Fe^{3+}/\sum Fe$, these components can then be linearly correlated with $Fe^{3+}/\sum Fe$ to produce a simple linear mixing model able to predict $Fe^{3+}/\sum Fe$ (Malherbe and Claverie, 2013; Vigneau et al., 1997). All that is required is that the PCA be performed simultaneously on the samples and standards so that the principal components form a common basis for each dataset. A decision still has to be made about how much of the spectrum to include to optimise the analysis, with practical limitations on analysis time meaning that we have here included only the pre-edge region (7105–7119 eV) for which we have the highest quality data (Table A.1). However, PCR is readily extensible to all parts of the spectrum

that are thought to contain information on oxidation state – with components describing effects uncorrelated with valence changes (such as noise) readily identified from the statistical insignificance of their associated parameters in the mixing model.

The result of the initial PCA for our combined dataset of sample and standard spectra is shown in Fig. 3 for the region 7105–7119 eV, which is useful as a visual description of why the PCR method works. Principal component 1 (PC1) effectively describes an average of the spectra studied which, given the abundance of sample spectra (64) compared to reference spectra (12), is relatively reduced (compare with spectra in Fig. 2B). Although PC1 describes a majority of the variance (99.6%), additional components are required to describe the systematic shifts in the pre-edge multiplet occurring with changing oxidation state. The component that most clearly creates the expected shifts in the pre-edge is PC2, which describes a peak at ~ 7114.5 eV that, when mixed with PC1, shifts the relative amplitude of the pre-edge multiplet to higher or lower energies. Taking a linear mixture of PC1 and PC2 is thus similar to the process of fitting the pre-edge with the Gaussian, Lorentzian and pseudo-Voigt functions of other calibration methods; however, PCA allows the data to define the best fitting form for the peaks, and no information is discarded as background.

Principal component analysis also offers a useful check of whether the reference spectra exhibit the same structural features as the unknowns, similar to using the pre-edge intensity and centroid energy (Wilke et al., 2001). This is particularly important given the potential for Fe coordination to influence the pre-edge structure of the spectra and for these structural effects to vary between natural and synthetic materials. We show the first two PCs from our dataset in Fig. 4. The overlap in PC1 and PC2 between the sample and reference spectra, combined with their similarity in centroid position and pre-edge intensity, is good evidence that the pre-edge structure in both sets of materials is varying in response to the same process: in this case the proportions of $Fe^{3+}/\sum Fe$.

After PCA, the next step is to perform the multiple linear regression of the selected PCs as predictors of $Fe^{3+}/\sum Fe$. To do this we have used the 'ols' function from the 'rms' package in the R statistical programming language (R Core Team, 2013), which carries out weighted ordinary least squares regression. We have used both PC1 and PC2 so as to incorporate information on the whole pre-edge region into the calibration. Applying this method, the form of the calibration to $Fe^{3+}/\sum Fe$ is:

$$Fe^{3+}/\sum Fe = a_0 + a_1 PC1 + a_2 PC2, \tag{2}$$

where a_0, a_1 & a_2 are the regression coefficients, and PC1 and PC2 the principal component scores for the spectra. We note that PC1 and PC2 could also have higher degree terms included in this equation; however, the improvement in fit from including these additional terms is not significant and does not change our results.

The multiple linear regression using both PC1 and PC2 is shown in Fig. A.1. The reduced chi-squared for this fit is 2.3, and remains almost constant if three or more components are used, indicating that the

calibration performs reasonably with just the first two components.

2.5. Precision

Over our analytical session we made four repeat analyses of the suite of NMNH 117393 reference glasses. In the final PCR calibration we used an average spectrum for each reference glass. However, we can also take each set of NMNH 117393 analyses separately and use these to calibrate the data for $Fe^{3+}/\sum Fe$. This acts as a test of the calibration's intra-session drift and stability. Recalibrating the data there is no evidence of drift within the session, nor significant variability depending upon the set of standard analyses chosen to perform the calibration. The 1σ precision calculated on $Fe^{3+}/\sum Fe$ from the different calibrations is $\sim 0.1\%$, more than an order of magnitude less than the systematic change we observe along-ridge towards Iceland. Repeat analyses of an in-house reference glass over the same period gave a 1σ reproducibility of 0.16%, which is the precision we quote in subsequent figures.

To estimate the uncertainty in the calibration that derives from the linear model fit to the Mössbauer data and the precision of the Mössbauer data itself, we have performed Monte Carlo modelling. The modelling starts with the raw spectra, randomly adds noise to the spectra assuming Poisson counting statistics on each point, re-performs PCR permuting each Mössbauer measurement of $Fe^{3+}/\sum Fe$ on the NMNH 117393 glasses by the uncertainty quoted in Cottrell and Kelley (2009), and then calculates a new set of calibration parameters. There is a high degree of correlation between the intercept (a_o) and coefficient for PC1 (a_1), indicating a trade-off in their influence on $Fe^{3+}/\sum Fe$. In contrast, the coefficient for PC2 (a_2) is largely independent of the value chosen for a_0 or a_1, as expected given the orthogonal basis provided by PCA.

Propagating the error matrix for the PCR calibration parameters through to $Fe^{3+}/\sum Fe$ using the general formula

$$\sigma^2 = \mathbf{p}\mathbf{\Sigma}^{\mathbf{a}}\mathbf{p}^{\mathsf{T}}, \tag{3}$$

gives an external 1σ precision of 0.4% (where $\mathbf{p}$ is the vector of principal component scores and $\mathbf{\Sigma}^{\mathbf{a}}$ is the covariance matrix for the model parameters, see Table A.2 for values). This precision is still less than half of the total along-ridge shift in $Fe^{3+}/\sum Fe$ we observe. However, for the remainder of this paper we use the external reproducibility of 0.16% as our error term on the data, since we are focusing on the relative difference between samples rather than systematic shifts that could result from error in the calibration.

3. Results

The 700 km transect of mantle represented by the Reykjanes Ridge samples incorporates both the long-wavelength transition from background MORB-like compositions in the south to strongly mantle plume-influenced in the north, and short-lengthscale heterogeneities in the form of seamounts (Murton et al., 2002). The raw $Fe^{3+}/\sum Fe$ from these samples is presented in Fig. 5A as a function of radial distance from

the Iceland plume centre (Shorttle and Maclennan, 2011). At any given distance, more evolved basalts with lower MgO are more oxidised than primitive basalts, confirming the importance of low pressure fractionation in modifying primary $Fe^{3+}/\sum Fe$ (Bézos and Humler, 2005; Cottrell and Kelley, 2011). Nevertheless, long-wavelength structure is apparent, with basalts at a similar MgO showing a progressive shift to higher $Fe^{3+}/\sum Fe$ closer to Iceland. The seamount 14D (labelled square symbols Fig. 5A) has also captured short-lengthscale heterogeneity, which, given its MgO, is as oxidised as basalts 700 km closer to Iceland.

3.1. Accounting for crystal fractionation

The sensitivity of $Fe^{3+}/\sum Fe$ to low pressure fractionation has been previously demonstrated in MORB suites analysed by XANES (Cottrell and Kelley, 2011). Four lines of evidence indicate that fractionation has also affected the Reykjanes Ridge suite of basalts studied here:

1. MgO concentrations of the Reykjanes Ridge glasses fall between 6.5 and 9 wt% MgO. Given that a primary MORB will have $\sim$ 10 wt% MgO, significant fractionation of at least olivine must have occurred in all these samples.
2. There is abundant petrological evidence from these samples of olivine macrocrysts, and in many cases plagioclase and clinopyroxene crystals (Murton, 1995).
3. Major element trends of Al and Ca with Mg (Fig. A.2), and trace element trends of Eu also indicate plagioclase and clinopyroxene fractionation (Murton et al., 2002).
4. It is clear from Fig. 5 and 6 that crystal fractionation has also played an important role in determining $Fe^{3+}/\sum Fe$ in Reykjanes Ridge magmas. $Fe^{3+}/\sum Fe$ is systematically higher at a given distance from the plume centre in the most evolved samples (those with lowest MgO) compared with more primitive basalts.

Crystal fractionation is therefore an important process in our Reykjanes Ridge dataset, as it is likely to be generating scatter in the along-ridge trend that is not associated with mantle source or processes. However, despite the need to correct $Fe^{3+}/\sum Fe$ for fractionation, we emphasise that the existence of long- and short-lengthscale variability in $Fe^{3+}/\sum Fe$ around Iceland is not predicated upon applying this correction to the data.

For the fractionation correction we tested both Petrolog (Danyushevsky and Plechov, 2011) reverse fractionation calculations, and two-stage empirical and olivine addition models (Figs. A.3 and A.2). Both methods gave very similar results and we chose the empirical method for its simplicity.

To apply any fractionation correction, an estimate is required of the MgO at which olivine-only crystallisation transitions to olivine + clinopyroxene + plagioclase crystallisation. We identified this point using an optimisation algorithm to find the MgO split that produces the two high- and low-MgO vs major element regressions with minimum misfit. The MgO found with this method was 8.0 wt%. Samples below 8.0 wt%

MgO had their major element compositions shifted parallel to a York (1969)-style fit to the low MgO data, until at 8 wt% MgO (Fig. 6). Further correction to 10 wt% MgO, or until the liquid was in equilibrium with Fo_{90}, was performed with simple olivine addition using the Herzberg and O'Hara (2002) model. The key result of applying this fractionation correction to the data is that it does not remove the sense of along-ridge shift to more oxidised compositions (Fig. 6).

3.2. The effect of degassing

From a mantle geochemical perspective, it is important to exclude the null hypothesis that the along-ridge trends in $Fe^{3+}/\sum Fe$ are a result of systematic along-ridge degassing. As the Reykjanes Ridge shallows, samples are erupted under progressively lower confining pressures, allowing for more syn-eruptive degassing prior to quenching. To account for the long-wavelength trend of increasing oxidation towards Iceland (Fig. 5B), degassing would need to: (1) involve a net transfer of electrons from the melt to the gas phase; and (2) involve the redox-influencing gas phase(s) beginning significant degassing over the depth interval where we observe an increase in basalt fO_2. Whether either of these conditions apply can be tested both empirically and with degassing models.

The long-wavelength trend of increasing oxidation towards Iceland is broken by the three most northerly samples (Fig. 5B). These basalts were erupted in the shallowest water (< 500 m) of the sample suite, and have $Fe^{3+}/\sum Fe$ $\sim$0.05 lower than the samples immediately to their south. The low pressure of eruption makes these samples the most likely to have experienced degassing,. Degassing of the most northerly samples is consistent with their lower S content compared with other samples (Fig. 7A, triangle symbols) and with their H_2O contents (Nichols et al., 2002), which are slightly lower than the trend of increasing H_2O towards Iceland would predict. Given the evidence for degassing, the offset of these samples to lower $Fe^{3+}/\sum Fe$ suggests that degassing has reduced them. If this is the case, then the longer wavelength trend of increasing oxidation towards Iceland is unlikely to be due to degassing, and therefore degassing as a null hypothesis cannot explain a majority of the data.

We can assess the influence of degassing on Reykjanes Ridge basalts with degassing models. As discussed above, the basalts erupted in water depths of < 500 m will have been the most strongly affected by H_2O and S loss, while CO_2 degassing will have been significant for all samples (Dixon et al., 1991). Of these volatile species, sulfur has the greatest potential leverage on magma redox state; this has been shown both theoretically (Burgisser and Scaillet, 2007) and in nature (Moussallam et al., 2014). Writing in terms of half

reactions, sulfur degassing could proceed by

$$S^{2-[melt]} \rightarrow S^{4+}O_2^{[gas]} + 6e^- \qquad \text{6 electrons transferred to melt,} \tag{4a}$$

$$S^{2-[melt]} \rightarrow H_2S^{2-[gas]} \qquad \text{no electron transfer,} \tag{4b}$$

$$S^{6+[melt]} + 2e^- \rightarrow S^{4+}O_2^{[gas]} \qquad \text{2 electrons transferred to gas,} \tag{4c}$$

$$S^{6+[melt]} + 8e^- \rightarrow H_2S^{2-[gas]} \qquad \text{8 electrons transferred to gas.} \tag{4d}$$

If we make the additional assumption that Fe, as the dominant heterovalent species in a melt, accommodates all the electron exchange, then these reactions are capable of producing large shifts in Fe oxidation state. The direction of redox change depends on the initial sulfur speciation in the liquid and the sulfur species formed in the gas phase, with sulfur degassing being capable of both reduction (Eq. 4a) and oxidation of magma (Eqs. 4c and 4d).

In nature, multiple sulfur degassing pathways will be exploited (e.g. Gaillard et al. (2011)); their relative importance as a function of melt composition and pressure will determine the net redox effect on the melt. A key parameter in determining the mode of sulfur degassing will be its speciation in the melt (Eqs. 4a–4d). For Reykjanes Ridge basalts with their measured ΔQFM from +0.3 to +0.6, S^{2-} will be the dominant sulfur species in the liquid (Jugo, 2009) (at this fO_2 a maximum of 10% of the S is in the S^{6+} state). Sulfur loss from these basalts as SO_2 will therefore reduce them (Eq. 4a), whereas sulfur loss as H_2S is redox neutral (Eq. 4b). The precise proportions of SO_2 and H_2S being lost from the melt will depend on the pressure and temperature of degassing, but the key point is that, provided S in the melt is dominantly S^{2-}, this degassing will be reducing. Fig. 7B shows a simple model implementing the redox stoichiometries outlined in Eqs. 4a–4d. Even in an unrealistically oxidising case where 30% of the sulfur in the melt is present as S^{6+} and degasses to 1:1 H_2S:SO_2, the basalts are reduced by degassing.

The results from our simple calculations (Fig. 7B) are confirmed when we correct for degassing with the full thermodynamic model of Gaillard et al. (2011), which predicts sulfur solubility and speciation in the liquid and gas phases. For these calculations we take the H_2O data from Nichols et al. (2002) and our measured fO_2. There are two important results from our application of the Gaillard et al. (2011) model: Firstly, it predicts significant sulfur loss only for basalts erupted in < 500 m water depth; therefore, most samples experienced insufficient S degassing to explain the oxidation trend observed for basalts erupted in 1000 m of water (Fig. 7C). Secondly, the Gaillard et al. (2011) model predicts that, at the oxidation state of the Reykjanes Ridge basalts (ΔQFM $\sim +0.5$), the molar ratio of degassing SO_2/H_2S is > 5 over all pressures considered (equivalent water depths from 300 m to > 1000 m). As a result, applying the model to correct $Fe^{3+}/\sum Fe$ in the four most degassed samples back to their pre-degassing (500 m water depth) values restores these samples to the long-wavelength trend of increasing oxidation towards Iceland (Fig. 7C).

In summary, neither the onset of significant degassing (at ~ 500 m water depth) nor its redox effect

(reducing) are consistent with the observed trend of basalts becoming more oxidised towards Iceland.

3.3. The fractionation corrected dataset

In the remainder of this paper we use the Reykjanes Ridge data corrected for fractional crystallisation, but uncorrected for degassing: we prefer to use the minimally corrected dataset that still shows significant structure and, as shown above, degassing will only have diminished the trend of along-ridge oxidation.

In the fractionation-corrected dataset the along-ridge transition to more oxidised samples closer to Iceland remains. However, the samples furthest from Iceland (> 1000 km) also appear to show a slight increase in $Fe^{3+}/\sum Fe_{(10)}$ compared with those at intermediate distances, creating a U-shaped along-ridge profile. This is true even excluding samples 17D1 and 14D.

The range of $Fe^{3+}/\sum Fe_{(10)}$ in the dataset, ~ 0.015, is equivalent to the range in global primitive MORB (Cottrell and Kelley, 2013) (Fig. 5B). This similarity in absolute variability found in Cottrell and Kelley (2013) and our regional dataset is also present when $Fe^{3+}/\sum Fe_{(10)}$ is used to calculate the basalts' oxygen fugacity as $\log(fO_2)$ with respect to QFM buffer, $\Delta QFM_{(10)}$ (Fig. 5C, Kress and Carmichael (1991)). Samples close to Iceland vary in fO_2 by ~ 0.25 $\log(fO_2)$ units, compared to ~ 0.3 $\log(fO_2)$ units in global primitive MORB (Cottrell and Kelley, 2013). Although the amplitude of redox shifts are similar, the major difference between the global MORB dataset (Cottrell and Kelley, 2013) and our dataset is that we find both trace element and isotopic enrichment to be consistently associated with oxidation. This relationship holds over the 100 km scale, where increases in incompatible trace element ratios (e.g. Zr/Y) and isotope ratios (e.g. $^{208}Pb/^{204}Pb$) match increasing $Fe^{3+}/\sum Fe_{(10)}$ (Fig. 5B and C); and is present on the 10 km scale of the enriched basalts sampled from seamount 14D.

Fractionation-corrected $Fe^{3+}/\sum Fe_{(10)}$ shows statistically significant correlations with the incompatible element enrichment recorded by trace element ratios and isotope systems (Fig. 8). Sample 17D1 was not included in the regression analysis of Fig. 8 because of its unique composition (Murton et al., 2002): despite relatively low La/Yb, Zr/Y, K_2O/TiO_2 and absolute incompatible element concentrations, 17D1 has high $^3He/^4He$ and is moderately oxidised. Whilst 17D1 may represent a distinct component within the plume mantle (Thirlwall et al., 2004), its geochemical characteristics are not reflected in the rest of the data so we do not consider this sample any further.

4. Discussion

4.1. The control of melting processes on basalt fO_2

Given the observed along-ridge oxidation towards Iceland (Fig. 5) and the correlation of this oxidation with lithophile element and radiogenic isotope tracers of enrichment (Fig. 8), the key question is what source or process relates enrichment to increased oxidation. One challenge we face is that the correlation

between source and mantle potential temperature inherent to our dataset, and many plume-scale transects of mantle/basalt chemistry, makes it difficult to identify causal relationships between enrichment, melting style and fO_2. However, by considering both the long- and short-lengthscale chemical structure along the Reykjanes Ridge we can begin to separate the roles of source and temperature.

The mantle potential temperature increases towards Iceland by $> 130°C$ (White et al., 1995; Shorttle et al., 2014), implying an associated increase in the mean pressure and extent of melting, and a higher pressure of initial solidus intersection. Higher mean extents of melting should cause $Fe^{3+}/\sum Fe_{(10)}$ to decrease towards Iceland, because Fe_2O_3 behaves moderately incompatibly during mantle melting (Canil et al., 1994). This process may in fact be controlling the slight northwards decrease in $Fe^{3+}/\sum Fe_{(10)}$ observed in the most distant samples (Fig. 5B): a region where the plume's thermal influence is present and increasing northwards, but the chemical signature may be weak (Shorttle et al., 2010; Jones et al., 2014). That increasing $Fe^{3+}/\sum Fe_{(10)}$ is also observed in the basalts erupted closest to Iceland indicates that some other process or source factor must come to dominate over the dilution of Fe_2O_3 by melting degree. This is also clear from the ratios (Fig. 5 and 8) and raw concentrations (Murton et al., 2002) of incompatible elements, which increase towards Iceland despite progressively higher extents of melting.

It is hard to reconcile the geochemistry of seamount 14D, which is oxidised and enriched, with changes in the temperature and pressure of melting as being the primary drivers of fO_2 variability along-ridge. On the lengthscale of seamount 14D, which is within 30 km of otherwise more reduced and depleted basalts on the southern Reykjanes Ridge, background temperature changes are likely to be minimal. As many of the geochemical characteristics of 14D are also the same as strongly plume-influenced basalts erupted closer to Iceland (Hilton et al., 2000; Murton et al., 2002; Thirlwall et al., 2004) it is likely that both the long- and short-lengthscale structure in fO_2 are explained by the same phenomenon. Only changes in source composition are likely to be present at high amplitude on both long and short lengthscales down the Reykjanes Ridge, and be capable of modifying both the oxidation state and isotope chemistry of basalts. (We note that 14D does not coincide with a V-shaped ridge crest or trough (Jones et al., 2014).)

Mantle potential temperature will also have an effect on ferric iron through its influence on the mineral and volatile assemblages buffering melting. If the source is graphite-buffered then higher pressures of initial melting towards Iceland could produce more oxidised basalts, as graphite leaves the residue earlier along the decompression path (Ballhaus and Frost, 1994). Taking the increase in the initial pressure of melting towards Iceland to be ~ 1 GPa (Shorttle et al., 2014), the earlier loss of graphite buffering under northern ridge segments could oxidise basalts by $\sim 0.4 \log(fO_2)$ units relative to those further south. However, both MORB and Reykjanes Ridge samples are too oxidised to be in equilibrium with a graphite-bearing source (Cottrell and Kelley, 2011). So a varying pressure of graphite exhaustion cannot be driving the observed changes in $Fe^{3+}/\sum Fe$ or $\Delta QFM_{(10)}$ between samples.

A separate role for mantle carbon influencing the oxidation state of erupted basalts has been proposed by

Cottrell and Kelley (2013) and Stagno et al. (2013), who considered how variations in the absolute amount of carbon between mantle domains may affect fO_2. In this model the redox melting of carbon to carbonate during decompression reduces the ferric iron in silicates leaving a more reduced source. As the carbon content of enriched mantle is (possibly) higher than that of ambient MORB mantle, enriched domains will produce more reduced silicate melts as more of their ferric iron is reduced during redox melting of carbon (Cottrell and Kelley, 2013). However, towards Iceland both the incompatible trace element content and $Fe^{3+}/\sum Fe_{(10)}$ of basalts increases. For example, the higher Nb content of near-Iceland basalts (Murton et al., 2002) could imply a mantle source 10-fold enriched in carbon with respect to MORB (Hauri et al., 2002). If this carbon underwent redox melting then we would expect the enriched basalts near Iceland (and the seamount 14D) to be the most reduced, the opposite to what is observed. Therefore, accounting for redox melting would imply a very oxidised enriched Icelandic source, so that following carbon oxidation the silicate residue could still produce melts oxidised relative to MORB.

Ultimately, understanding the effect of simple changes in melt region parameters on the oxidation state of aggregate basalts will require more comprehensive thermodynamic models of mantle melting. These models face a significant challenge in needing to incorporate carbon-sulfur-silicate buffering in addition to silicate phase changes and pressure-dependent solid solutions. However, with our current understanding of melt region redox processes it appears likely that an intrinsically oxidised component is required in the Icelandic mantle to explain the relationships seen in Figs. 5 and 8.

4.2. The origin of an enriched and oxidised Icelandic source component

To relate our observations to solid Earth oxygen fluxes, an important question is how the enriched Icelandic source became oxidised. One possibility is that this occurred by metasomatic enrichment, either through carbonatitic fluids as has been suggested for lithospheric peridotites (Canil et al., 1994), or via hydrous metasomatism as may occur at subduction zones (Kelley and Cottrell, 2009). Whilst it difficult to place unique constraints on the origin of enriched sources (especially as the process may have been polyphase), we can assess each metasomatic mechanism for consistency with other major and trace element data.

Canil et al. (1994) found that carbonatitic metasomatism, in addition to raising fO_2, raised CaO/Al_2O_3 in peridotites. However, this major element signal of carbonatite interaction is the opposite of what we see in enriched Icelandic basalts Shorttle and Maclennan (2011).

The second possibility is that the Icelandic source was enriched in a subduction zone setting, transferring both fluid-mobile trace elements and high fO_2, as is inferred to be happening beneath modern arcs Kelley and Cottrell (2009). To address this we have calculated the apparent relative compatibility of Fe_2O_3 and trace elements in our sample suite (Fig. 9A, Sims and DePaolo (1997); Hémond et al. (2006); Stracke et al. (2003a)). In the case of metasomatic hydrous enrichment we would expect: 1. fluid-mobile elements such

as Sr, Pb, U, Cs, Rb and Ba to be relatively enriched compared with less fluid-mobile trace elements of similar solid–melt partitioning (as indicated by high gradients in log(element) vs. log(Fe_2O_3) space); 2. for Fe_2O_3 to show the strongest correlation with these fluid-mobile elements; and 3. apparent Fe_2O_3 partition coefficients much less than the bulk $D_{Fe_2O_3} = 0.1$ predicted for peridotite (O'Neill et al., 1993; Canil et al., 1994). However, Fig. 9A shows that the apparent partition coefficient for Fe_2O_3 is most similar to that of Gd (~ 0.1), consistent with predicted solid–melt equilibria. The correlations between Fe_2O_3 and fluid-mobile elements, although high, are also weaker than for similarly incompatible non-fluid-mobile elements. And despite being enriched, the fluid-mobile elements are in fact less enriched than would be expected given their very low partition coefficients during peridotite melting.

Following the reasoning above we reject the possibility that oxidised hydrous/carbonatitic fluids/melts were important in generating the enriched Icelandic source characteristics. Instead, given the evidence for pyroxenitic components in the Iceland plume source (Chauvel and Hémond, 2000; Stracke et al., 2003b; Shorttle and Maclennan, 2011; Sims et al., 2013), we instead consider that the enriched oxidised component is ancient recycled seafloor. Oceanic crust will be enriched in Fe_2O_3 relative to ambient mantle simply by ferric iron's incompatibility during partial melting, but significant secondary enrichment may also occur during hydrothermal alteration through sulfate reduction at the ridge axis (Lécuyer and Ricard, 1999; Sleep, 2005). De-watering of the slab during subduction could then account for the relative under-enrichment of fluid-mobile trace elements in the enriched Icelandic source (Fig. 9B).

4.3. Estimating the ferric iron content of enriched Icelandic mantle

None of the melt compositions in the Reykjanes Ridge suite are representative pure melts of single mantle domains. Instead they will be mixtures of melts from the enriched pyroxenitic and depleted lherzolitic Icelandic source components (Shorttle and Maclennan, 2011; Shorttle et al., 2014). Therefore, to constrain the origin of the enriched oxidised component we first need to estimate its Fe_2O_3, which will be more extreme than is recorded in any basalts we have sampled.

To determine Fe_2O_3 in primitive melts from the enriched source we have regressed $Fe_2O_{3(Fo90)}$ (ferric iron corrected to be in equilibrium with Fo_{90} olivine) from our samples against an estimate of the proportion of pyroxenite-derived melt contributing to their bulk chemistry (Fig. 10). The calculations to determine the pyroxenite-derived melt fraction in Icelandic plume basalts have been discussed in detail by Shorttle et al. (2014): the basic reasoning is that the chemical diversity of sampled basalts from onland Iceland makes it possible to identify the enriched and depleted endmember melt compositions being supplied from the mantle. These endmember melt compositions can then be used to form a mass balance to produce the incompatible trace element chemistry of derivative mixed melts, thus constraining the proportion of each endmember melt in the mixture. The intersection of the regression in Fig. 10A with the $Fe_2O_{3(Fo90)}$ axis at 100% pyroxenite-derived melt constrains the $Fe_2O_{3(Fo90)}$ in primary melts of the enriched Icelandic source

to be $\sim$ 1.8 wt%–2.0 wt%. Depleted melt compositions are assumed to be represented by the most depleted basalts along the Reykjanes Ridge (at 0% pyroxenite-derived melt) with $Fe_2O_{3(Fo90)} \sim 1.5$ wt%.

We next need to project this melt composition into an estimate of ferric iron in the source ($[Fe_2O_3]_{(source)}$). For this we use the aggregate fractional melting equation $C_l = C_0(1/F(1-(1-F)^{(1/D_{Fe_2O_3})}))$, where C_l is the liquid composition, C_0 the solid composition, F the melt fraction, and $D_{Fe_2O_3}$ the bulk ferric iron partition coefficient. We calculate bulk partition coefficients from the mineral–melt partition coefficients given in Mallmann and O'Neill (2009) and considering garnet–melt partition coefficients between 0.85 and 1. We take a source mineralogy for the depleted Icelandic source component of a spinel lherzolite (Shorttle and Maclennan, 2011), sp_2:ol_{55}:opx_{25}:cpx_{18} (spinel:olivine:orthopyroxene:clinopyroxene). Two mineral modes are tested for the pyroxenitic lithology (Shorttle and Maclennan, 2011; Kogiso et al., 1998): a garnet-bearing source gt_{27}:ol_{23}:cpx_{50} (gt = garnet) and a spinel-bearing source sp_7:ol_{18}:opx_{15}:cpx_{60}. These source mineralogies and partition coefficients are then combined to produce the range of bulk Ds in Table A.3, of which the extremes are used in calculating the bounds on our estimates of source Fe_2O_3. Melt fractions used in the calculations are taken from the model results of Shorttle et al. (2014), as reasonable estimates of mean degree of melting of peridotite and pyroxenitic lithologies given the requirement to match along-ridge crustal thicknesses (Smallwood and White, 1998; Navin and Sinha, 1998). The combination of melt fractions and partition coefficients used to produced the preferred and upper and lower bounds for each lithology in Fig. 10 are given in Table A.4.

Fig. 10B shows that whilst the depleted basalts in our dataset are well matched by melting of a typical upper mantle peridotite with $Fe_2O_3 = 0.3$ wt%, the enriched source must contain between 0.9 and 1.4 wt% Fe_2O_3. This Fe_2O_3 range falls between sources containing regular MORB and (oxidised) altered oceanic crust (Fig. 10C). Although our calculations cannot uniquely identify the source composition, they illustrate the key parameters that need to be constrained to arrive at a source estimate.

4.4. Implications for oxygen cycling

The results above leave open the possibility of the solid Earth having an important role in oxygen cycling through the subduction of altered oxidised oceanic crust which is eventually remelted at plume settings such as Iceland. Oxidation of the seafloor during hydrothermal circulation has only been efficient since global surface oxygenation generated appreciable sulfate concentrations in the oceans (Sleep, 2005; Kasting, 2013). Some estimates of the age of the enriched component in the Icelandic source place it at $\sim$ 400 Ma (McKenzie et al., 2004; Thirlwall et al., 2004), consistent with the requirement for oxic conditions to have been present in the deep ocean at the time of the source's formation (Canfield et al., 2007). The present-day eruption of oxidised basalts from the Iceland plume may therefore represent closure of the global oxygen cycle as envisaged by Lécuyer and Ricard (1999), as oxygen sequestered into the solid Earth by subduction is returned to the surface environment.

5. Conclusions

A suite of 64 Reykjanes Ridge basalts sampling long- and short-wavelength chemical and isotopic structure in the Iceland plume record changes in oxidation that correlate with enrichment: enriched basalts from closest to the Iceland plume and from a seamount with a plume geochemical affinity, have higher $Fe^{3+}/\sum Fe$ by up to 0.015 and higher ΔQFM by 0.25 $\log(fO_2)$ units. This trend is unlikely to be explained by degassing or crystallisation processes and is the opposite of what would be expected from redox melting of enriched high-carbon mantle domains. Instead, it is likely the positive correlation between oxidation and enrichment reflects the presence of intrinsically oxidised sources in the Icelandic mantle.

Fluid-mobile trace elements are under-enriched in near-plume Reykjanes Ridge basalts with respect to other incompatible elements, given their nominal silicate-melt partition coefficients. In addition to abundant evidence for the presence of recycled material in the Icelandic mantle, the relative under-enrichment of fluid-mobile elements suggests that enriched Icelandic mantle may have been hydrated at a ridge axis, followed by dehydration (and fluid-mobile element loss) during recycling. This ancient ridge axis hydration event, if it happened in the last 600 Ma, will have led to significant oxidation of the oceanic crust. Recycling of this component then introduces trace element-enriched and oxidised material back into the mantle.

By connecting ridge axis oxidation processes to recycling and eventual resampling by mantle plumes, our results are consistent with a role for the solid Earth in long-term oxygen cycling.

6. Acknowledgements

OS was supported by a Title A Fellowship from Trinity College, JM through NERC grant NE/J021539/1 and MH acknowledges a Junior Research Fellowship from Murray Edwards College, Cambridge. We acknowledge Diamond Light Source for time on beamline I18 under proposals SP9446, SP9456 and SP12130 and the support during our analytical sessions from beamline scientist Konstantin Ignatyev and principal beamline scientist Fred Mosselmans. The Smithsonian Institution National Museum of Natural History is thanked for their loan of NMNH 117393.

References

Bajt, S., Sutton, S.R., Delaney, J.S., 1994. X-ray microprobe analysis of iron oxidation states in silicates and oxides using X-ray absorption near edge structure (XANES). Geochimica et Cosmochimica Acta 58, 5209–5214.

Ballhaus, C., Frost, B.R., 1994. The generation of oxidised CO_2-bearing basaltic melts from reduced CH_4-bearing upper mantle sources. Geochimica et Cosmochimica Acta 58, 4931–4940.

Berry, A.J., O'Neill, H.S., Jayasuriya, K.D., Campbell, S.J., Foran, G.J., 2003. XANES calibrations for the oxidation state of iron in silicate glass. American Mineralogist 88, 967–977.

Bézos, A., Humler, E., 2005. The $Fe^{3+}/\sum Fe$ ratios of MORB glasses and their implications for mantle melting. Geochimica et Cosmochimica Acta 69, 711–725.

475 Burgisser, A., Scaillet, B., 2007. Redox evolution of a degassing magma rising to the surface. Nature 445, 194–197.
476 Canfield, D.E., Poulton, S.W., Narbonne, G.M., 2007. Late-Neoproterozoic deep-ocean oxygenation and the rise of animal life.
477 Science 315, 92–95.
478 Canil, D., O'Neill, H.S.C., Pearson, D.G., Rudnick, R.L., McDonough, W.F., Carswell, D.A., 1994. Ferric iron in peridotites
479 and mantle oxidation states. Earth and Planetary Science Letters 123, 205–220.
480 Carmichael, I.S.E., 1991. The redox states of basic and silicic magmas: a reflection of their source regions? Contributions to
481 Mineralogy and Petrology 106, 129–141.
482 Chase, C.G., 1981. Oceanic island Pb: two-stage histories and mantle evolution. Earth and Planetary Science Letters 52,
483 277–284.
484 Chauvel, C., Hémond, C., 2000. Melting of a complete section of recycled oceanic crust: Trace element and Pb isotopic evidence
485 from Iceland. Geochemistry, Geophysics, Geosystems 1.
486 Cottrell, E., Kelley, K.A., 2009. High-precision determination of iron oxidation state in silicate glasses using XANES. Chemical
487 Geology 268, 169–179.
488 Cottrell, E., Kelley, K.A., 2011. The oxidation state of Fe in MORB glasses and the oxygen fugacity of the upper mantle.
489 Earth and Planetary Science Letters 305, 279–282.
490 Cottrell, E., Kelley, K.A., 2013. Redox heterogeneity in mid-ocean ridge basalts as a function of mantle source. Science 340,
491 1314–1317.
492 Danyushevsky, L.V., Plechov, P., 2011. Petrolog3: integrated software for modeling crystallization processes. Geochemistry
493 Geophysics Geosystems 12.
494 Dixon, J.E., Clague, D.A., Stolper, E.M., 1991. Degassing history of water, sulfur, and carbon in submarine lavas from Kilauea
495 volcano, Hawaii. Journal of Geology 99, 371–394.
496 Farges, F., Lefrère, Y., Rossano, S., Berthereau, A., Calas, G., Jr., G.E.B., 2004. The effect of redox state on the local
497 structural environment of iron in silicate glasses: a combined XAFS spectroscopy, molecular dynamics, and bond valence
498 study. Journal of Non-Crystalline Solids 344, 176–188.
499 Frost, B.R., 1991. An introduction to oxygen fugacity and its petrological importance, in: Lindsley, D.H. (Ed.), Oxide minerals:
500 Petrologic and magnetic significance. Mineralogical Society of America, Washington DC. volume 25 of *Reviews in Mineralogy*
501 *and Geochemistry*, pp. 1–9.
502 Gaillard, F., Scaillet, B., Arndt, N.T., 2011. Atmospheric oxygenation caused by a change in volcanic degassing processes.
503 Nature 478, 229–232.
504 Gibson, S.A., Geist, D., 2010. Geochemical and geophysical estimates of lithospheric thickness variation beneath Galápagos.
505 Earth and Planetary Science Letters 300, 275–286.
506 Hauri, E., Gronvöld, K., Oskarsson, N., McKenzie, D., 2002. Abundance of carbon in the Icelandic mantle: constraints from
507 melt inclusions, in: AGU Spring Meeting Abstracts, p. 03.
508 Hémond, C., Hofmann, A.W., Vlastélic, I., Nauret, F., 2006. Origin of MORB enrichment and relative trace element compati-
509 bilities along the Mid-Atlantic Ridge between 10° and 24°N. Geochemistry Geophysics Geosystems 7.
510 Herzberg, C., O'Hara, M.J., 2002. Plume-associated ultramafic magmas of Phanerozoic age. Journal of Petrology 43, 1857–1883.
511 Hilton, D.R., Thirlwall, M.F., Taylor, R.N., Murton, B.J., Nichols, A., 2000. Controls on the magmatic degassing along the
512 Reykjanes Ridge with implications for the helium paradox. Earth and Planetary Science Letters 183, 43–50.
513 Jones, S.M., Murton, B.J., Fitton, J.G., White, N.J., Maclennan, J., Walters, R.L., 2014. A joint geochemical-geophysical
514 record of time-dependent mantle convection south of Iceland. Earth and Planetary Science Letters 386, 86–97.
515 Jugo, P.J., 2009. Sulfur content at sulfide saturation in oxidized magmas. Geology 37, 415–418.
516 Kasting, J.F., 2013. What caused the rise of atmospheric O_2. Chemical Geology 362, 13–25.
517 Kelley, K.A., Cottrell, E., 2009. Water and the oxidation state of subduction zone magmas. Science 325, 605–607.

Kessel, R., Schmidt, M.W., Ulmer, P., Pettke, T., 2005. Trace element signature of subduction–zone fluids, melts and supercritical liquids at 120–180 km depth. Nature 437, 724–727.

Kogiso, T., Hirose, K., Takahashi, E., 1998. Melting experiments on homogeneous mixtures of peridotite and basalt: application to the genesis of ocean island basalts. Earth and Planetary Science Letters 162, 45–61.

Kress, V.C., Carmichael, I.S.E., 1991. The compressibility of silicate liquids containing Fe_2O_3 and the effect of composition, temperature, oxygen fugacity and pressure on their redox states. Contributions to Mineralogy and Petrology 108, 82–92.

Lécuyer, C., Ricard, Y., 1999. Long-term fluxes and budget of ferric iron: implication for the redox states of the Earth's mantle and atmosphere. Earth and Planetary Science Letters 165, 197–211.

Liu, Y., Samaha, N.T., Baker, D.R., 2007. Sulfur concentration at sulfide saturation (SCSS) in magmatic silicate melts. Geochimica et Cosmochimica Acta 71, 1783–1799.

Malherbe, J., Claverie, F., 2013. Toward chromium speciation in solids using wavelength dispersive X-ray fluorescence spectrometry Cr Kβ lines. Analytica Chimica Acta 773, 37–44.

Mallmann, G., O'Neill, H.S.C., 2009. The crystal/melt partitioning of V during mantle melting as a function of oxygen fugacity compared with some other elements (Al, P, Ca, Sc, Ti, Cr, Fe, Ga, Y, Zr and Nb). Journal of Petrology 50, 1765–1794.

Manceau, A., Gorshkov, A.I., Drits, V.A., 1992. Structural chemistry of Mn, Fe, Co, and Ni in manganese hydrous oxides: Part I. information from XANES spectroscopy. American Mineralogist 77, 1133–1143.

McKenzie, D., Stracke, A., Blichert-Toft, J., Albaréde, F., Grönvold, K., O'Nions, R.K., 2004. Source enrichment processes responsible for isotopic anomalies in oceanic island basalts. Geochimica et Cosmochimica Acta 68, 2699–2724.

Métrich, N., Berry, A.J., O'Neill, H.S., Susini, J., 2009. The oxidation state of sulfur in synthetic and natural glasses determined by X-ray absorption spectroscopy. Geochimica et Cosmochimica Acta 73, 2382–2399.

Moussallam, Y., Oppenheimer, C., Scaillet, B., Gaillard, F., Kyle, P., Peters, N., Hartley, M., Berlo, K., Donovan, A., 2014. Tracking the changing oxidation state of Erebus magmas, from mantle to surface, driven by magma ascent and degassing. Earth and Planetary Science Letters 393, 200–209.

Murton, B.J., 1995. RSS Charles Darwin Cruise 80, 01 September to 01 October 1993. The PETROS programme: geologic sampling and bathymetric surveying of the Reykjanes Ridge between 57°N and 63°N, southwest of Iceland. Deacon Laboratory Cruise Report 236. Institute of Oceanographic Sciences.

Murton, B.J., Taylor, R.N., Thirlwall, M.N., 2002. Plume-ridge interaction: a geochemical perspective from the Reykjanes Ridge. Journal of Petrology 43, 1987–2012.

Navin, D.A., Sinha, M.C., 1998. The RAMESSES experiment–II. Evidence for accumulated melt beneath a slow spreading ridge from wide-angle refreaction and multichannel reflection seismic profiles. Geophysics Journal International 135, 746–772.

Nichols, A.R.L., Carroll, M.R., Höskuldsson, A., 2002. Is the Iceland hot spot also wet? evidence from the water contents of undegassed submarine and subglacial pillow basalts. Earth and Planetary Science Letters 202, 77–87.

O'Neill, H.S.C., Rubie, D.C., Canil, D., Geiger, C.A., II, C.R.R., Seifert, F., Woodland, A.B., 1993. Ferric iron in the upper mantle and in transition zone assemblages: implications for relative oxygen fugacities in the mantle. American Geophysical Union Geophysical Monograph 74, 73–88.

Press, W.H., Teukolsky, S.A., Vetterling, W.T., Flannery, B.P., 1992. Numerical Recipes in C, Second Edition. Cambridge University Press.

R Core Team, 2013. R: A Language and Environment for Statistical Computing. R Foundation for Statistical Computing. Vienna, Austria.

Schilling, J.G., 1973. Iceland mantle plume: Geochemical study of Reykjanes ridge. Nature 242, 565–571.

Shorttle, O., Maclennan, J., 2011. Compositional trends of Icelandic basalts: Implications for short-lengthscale lithological heterogeneity in mantle plumes. Geochemistry, Geophysics, Geosystems 12.

Shorttle, O., Maclennan, J., Jones, S.M., 2010. Control of the symmetry of plume ridge interaction by spreading-ridge geometry.

561 Geochemistry, Geophysics, Geosystems 11.
562 Shorttle, O., Maclennan, J., Lambart, S., 2014. Quantifying lithological variability in the mantle. Earth and Planetary Science
563 Letters 395, 24–40.
564 Sims, K.W.W., DePaolo, D.J., 1997. Inferences about mantle magma sources from incompatible element concentration ratios
565 in oceanic basalts. Geochimica et Cosmochimica Acta 61, 765–784.
566 Sims, K.W.W., Maclennan, J., Blichert-Toft, J., Mervine, E.M., Blusztajn, J., Gönvold, K., 2013. Short length scale mantle
567 heterogeneity beneath Iceland probed by glacial modulation of melting. Earth and Planetary Science Letters 379, 146–157.
568 Sleep, N.H., 2005. Dioxygen over geologic time. Metal Ions in Biological Systems 43, 49–73.
569 Smallwood, J.R., White, R.S., 1998. Crustal accretion at the Reykjanes Ridge, 61°–62°n. Journal of Geophysical Research
570 103, 5185–5201.
571 Stagno, V., Ojwang, D.O., McCammon, C.A., Frost, D.J., 2013. The oxidation state of the mantle and the extraction of carbon
572 from the Earth's interior. Nature 493, 84–88.
573 Stracke, A., 2012. Earth's heterogeneous mantle: a product of convection driven interaction between crust and mantle. Chemical
574 Geology 330–331, 274–299.
575 Stracke, A., Bizimis, M., Salters, V.J.M., 2003a. Recycling oceanic crust: quantitative constraints. Geochemistry, Geophysics,
576 Geosystems 4.
577 Stracke, A., Zindler, A., Salters, V.J.M., McKenzie, D., Blichert-Toft, J., Albarède, F., Grönvold, K., 2003b. Theistareykir
578 revisited. Geochemistry, Geophysics, Geosystems 4.
579 Thirlwall, M.F., Gee, M.A.M., Taylor, R.N., Murton, B.J., 2004. Mantle components in Iceland and adjacent ridges investigated
580 using double-spike Pb isotope ratios. Geochimica et Cosmochimica Acta 68, 361–386.
581 Vigneau, E., Devaux, M.F., Qannari, E.M., Robert, P., 1997. Principal component regression, ridge regression and ridge
582 principal component regression in spectroscopy calibration. Journal of Chemometrics 11, 239–249.
583 White, R.S., Bown, J.W., Smallwood, J.R., 1995. The temperature of the Iceland plume and origin of outward-propagating
584 V-shaped ridges. Journal of the Geological Society of London 152, 1039–1045.
585 Wilke, M., Farges, F., Petit, P.E., Jr., G.E.B., Martin, F., 2001. Oxidation state and coordination of Fe in minerals: An Fe
586 K-XANES spectroscopic study. American Mineralogist 86, 714–730.
587 Wilke, M., Jugo, P.J., Klimmm, K., Susini, J., Botcharnikov, R., Kohn, S.C., Janousch, M., 2008. The origin of S^{4+} detected
588 in silicate glasses by XANES. American Mineralogist 93, 235–240.
589 Wong, J., Lytle, F.W., Messmer, R.P., Maylotte, D.H., 1984. K-edge absorption spectra of selected vanadium compounds.
590 Physical Review B 30, 5596–5610.
591 York, D., 1969. Least squares fitting of a straight line with correlated errors. Earth and Planetary Science Letters 5, 320–324.

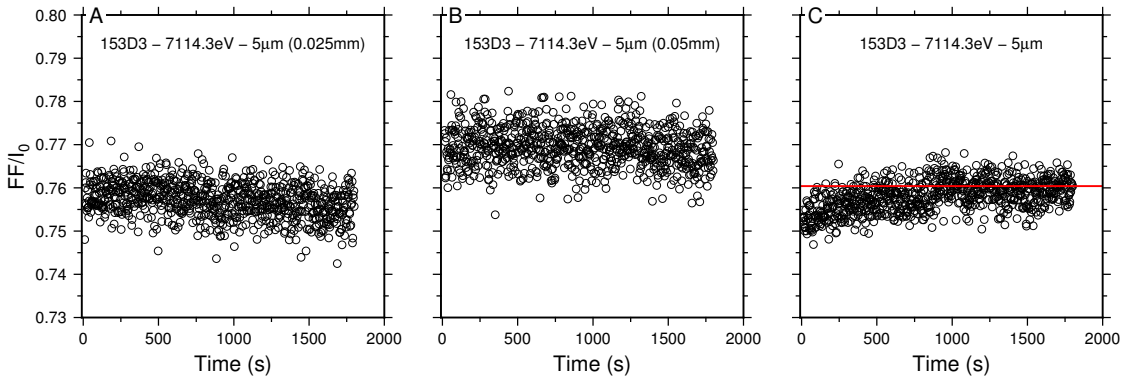

Figure 1: Time series of I_0 normalised fluoresced intensity (FF) at 7114.3 eV, the energy of the oxidised peak of the pre-edge doublet. This test was performed to determine whether there was time-dependent sample damage from exposure to the high energy X-ray beam. The test was performed at the same beam conditions as our analyses on natural Reykjanes Ridge basalt sample 153D3. A fresh spot on the sample was illuminated with a 5 μm diameter beam and the fluoresced intensity integrated over 1 s intervals. Plots A-C record, respectively, the time series produced for illumination from a beam attenuated with a 0.025 mm Al plate, 0.05 mm Al plate, and with no attenuation. In C, the red line marks the FF/I_0 at 7114.3 eV from a subsequent full spectrum acquisition ($\sim$ 30 minutes).

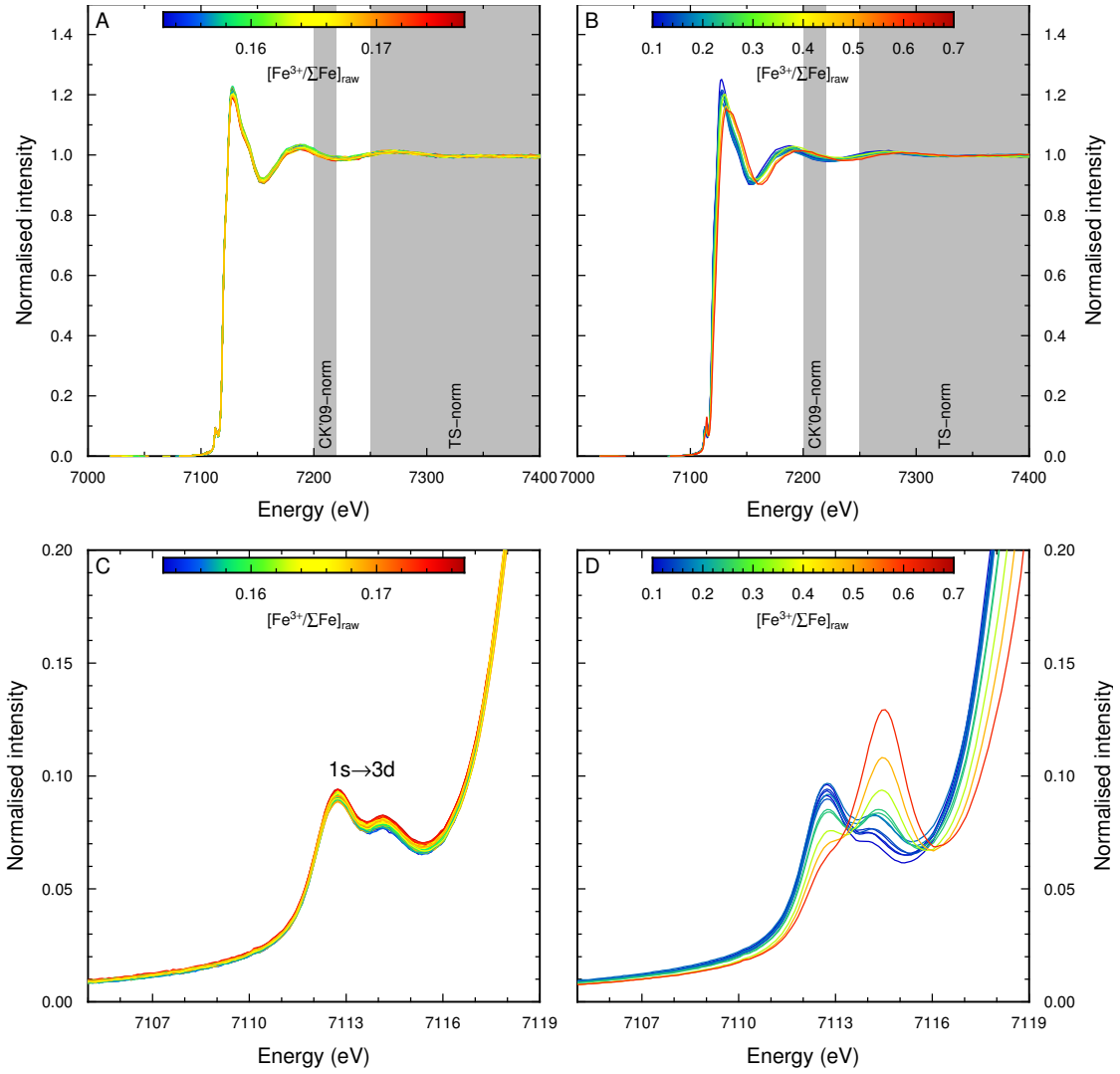

Figure 2: Edge-step normalised intensity vs. energy for sample and reference spectra. (a) and (b) show the full spectra collected from samples and standards (NMNH 117393, (Cottrell and Kelley, 2009)) respectively, with the energy range used in this study for normalisation marked on as the grey band 'TS-norm' and the energy range used by Cottrell and Kelley (2009) marked on as 'CK'09-norm'. Spectra have been coloured by their $Fe^{3+}/\sum Fe$ as determined from the XANES analyses (in the case of the reference glasses, this $Fe^{3+}/\sum Fe$ is effectively the reference value as determined by Mössbauer). (c) and (d) show spectra over the energy range of the pre-edge region we used in fitting the spectra from the samples and standards respectively. Over the pre-edge region, counting times were 5–10 s and energy steps were 0.1 eV.

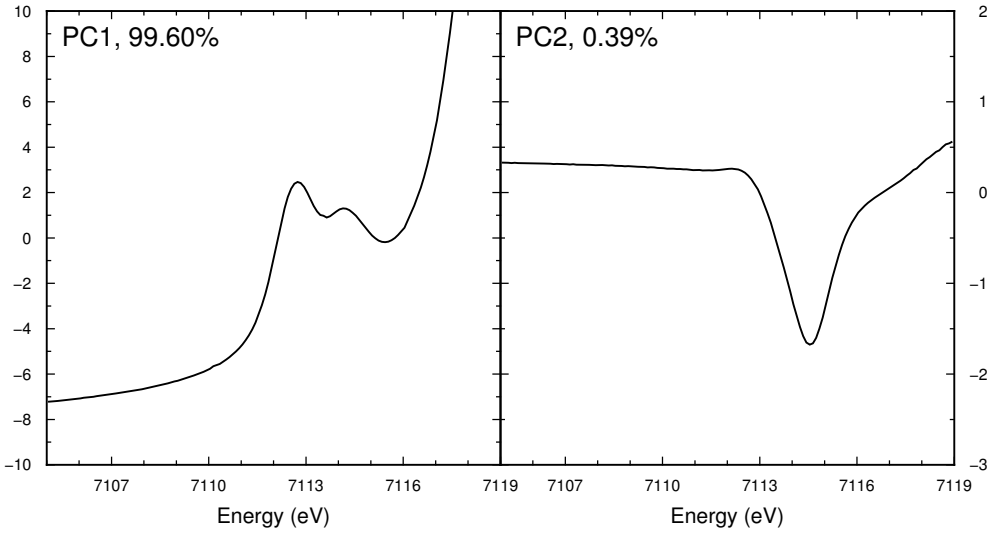

Figure 3: Projection of the first two principal components (PC1 and PC2) into energy space, showing how the principal components combine to reproduce the pre-edge structure of the sample and standard spectra. PC1 effectively represents an average spectrum which, because of the larger number of samples compared with standards, exhibits the spectral features of the 1s–3d transition in a glass with $Fe^{3+}/\sum Fe \sim 0.15$, i.e. roughly the ferric iron content of the natural glasses in our study. The second principal component consists of a peak at ~ 7114.5 eV that, when mixed in with PC1, can add to or subtract from the second peak in PC1, creating the pre-edge structure of the more oxidising reference glasses (compare with Fig. 2D). In contrast, higher components begin to show dominantly high frequency structure indicating that they are largely mapping noise.

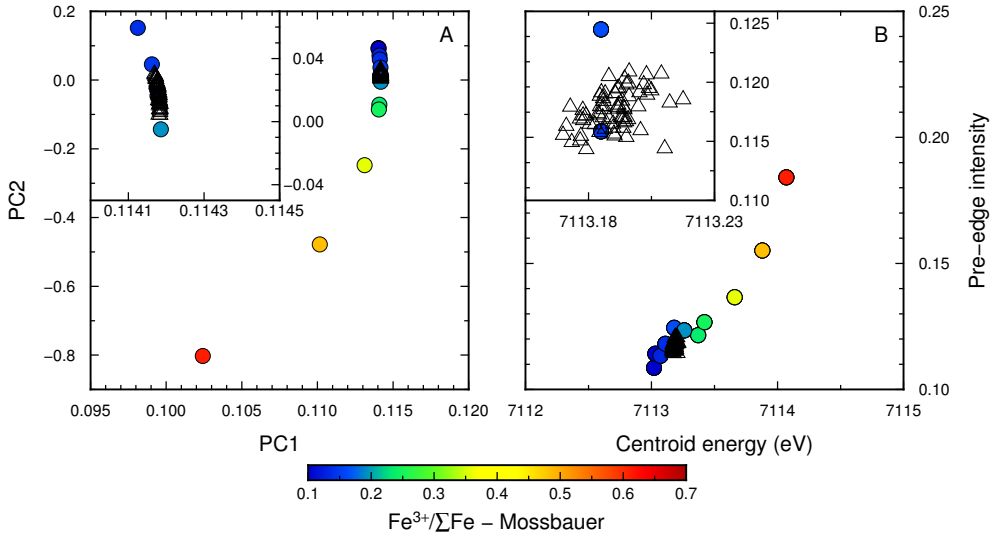

Figure 4: Assessment of spectral similarity between the samples and standards. (A) The PC1 and PC2 scores from sample spectra are plotted as open triangles and reference spectra from reference block NMNH 117393 as circles coloured by their $Fe^{3+}/\sum Fe$ (Cottrell and Kelley, 2009). Inset shows a magnification of the region occupied by the samples. (B) Centroid energies and pre-edge intensities calculated for the same reference and sample spectra. Samples and standards overlap in PC1-PC2 and centroid energy-pre-edge intensity, indicating the validity of, 1) projecting the principal component scores of the samples to $Fe^{3+}/\sum Fe$ using linear mixing of the known standard glasses, and 2) using the standards to calibrate the unknowns.

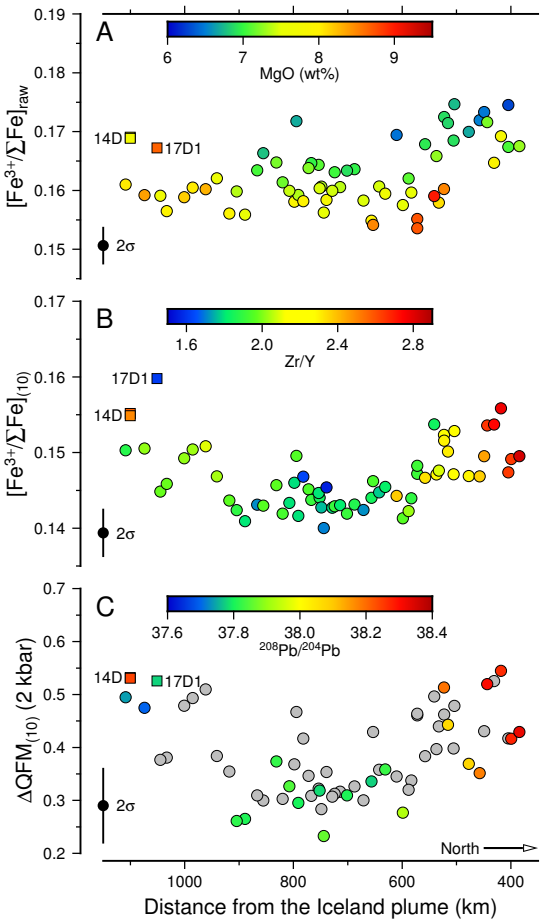

Figure 5: The along-ridge increase in $Fe^{3+}/\sum Fe$ and oxidation approaching Iceland. (A) Raw $Fe^{3+}/\sum Fe$ is plotted as a function of radial distance from the Iceland plume centre, and coloured by the MgO content of the sample glasses. Labelled square symbols are the samples identified as exhibiting geographically anomalous geochemical signals, of which the two 14D samples are enriched basalts from a seamount (Murton et al., 2002). (B) $Fe^{3+}/\sum Fe$ after correction for low pressure fractionation to 10 wt% MgO, with points coloured by Zr/Y. (C) Samples have been projected to their $\log(fO_2)$ relative to the QFM buffer at 2 kbar using the equation of Kress and Carmichael (1991); points are coloured by their Pb isotopic composition. In each panel the transition to more oxidised compositions occurs at ~ 600 km, concurrent with increases in indices of mantle enrichment such as Zr/Y and $^{208}Pb/^{204}Pb$. Trace element and isotope data from Murton et al. (2002); Thirlwall et al. (2004).

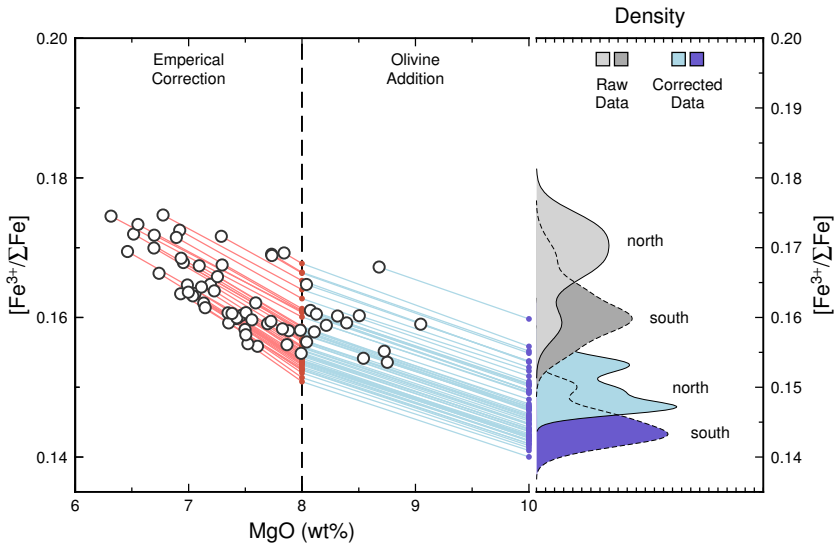

Figure 6: The path of reverse fractional crystallisation applied to the Reykjanes Ridge samples. The starting chemistry of each sample is marked by an open circle and the lines extending to higher MgO mark the reverse fractional crystallisation path. Samples with less than 8 wt% MgO were first corrected back to 8 wt% MgO by best-fit regression to their major element data. This empirical correction accounts for liquid fractionation in the olivine + plagioclase + clinopyroxene (i.e. gabbro) field. Subsequent reverse fractionation from 8 wt% MgO to 10 wt% MgO is performed by olivine addition using the Herzberg and O'Hara (2002) model. The side panel presents kernel density estimates of the dataset split into samples from the northern sector of the Reykjanes Ridge ($> 61.5°$ N and within 480 km of the plume centre, solid lines with grey fill) and samples from the southern sector ($\leq 61.5°$N and further than 480 km from the plume centre, dashed lines with no fill). Thin lines are the kernel density estimates for the raw dataset (open circles), whilst thick lines are for the data with the fractionation correction applied. For both the raw and corrected data basalts from the southern sector of the ridge are less oxidised than those from the northern sector.

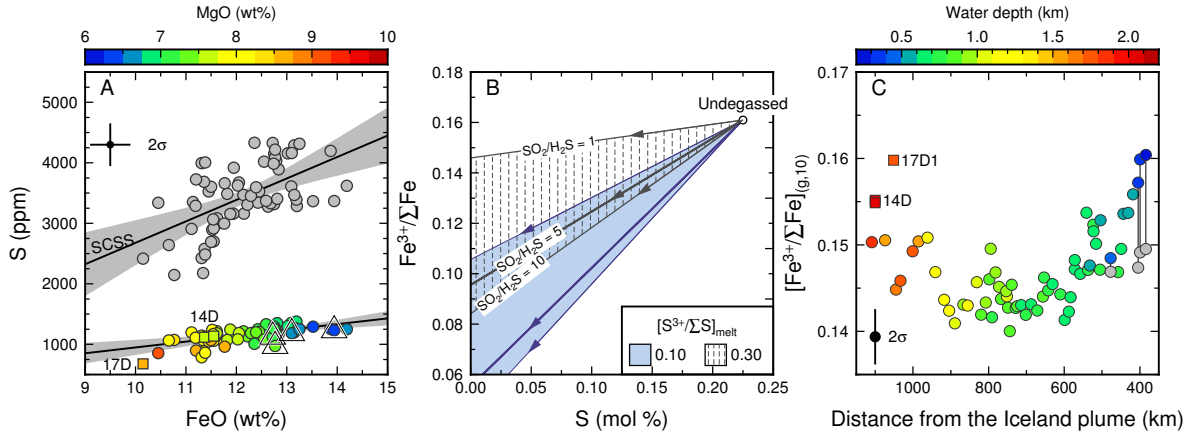

Figure 7: A quantification of how S degassing may have affected the redox state of Reykjanes Ridge basalts. (A) The sulfur content of samples plotted against their iron content (symbols coloured by MgO), with a regression and 95% confidence envelope. Samples erupted in less than 500 m water depth have a triangle plotted over them. The correlation between S and FeO implies that basalts may be sulfide saturated. However, calculating the predicted sulfur content at sulfide saturation (Liu et al., 2007) assuming T = 1100°C and P = 1000 bar (grey symbols) implies that the samples are undersaturated in sulfur. (C) A simple model investigating the effects of Eqs. 4a–4d on the oxidation state of the liquid during sulfur degassing. Degassing calculations are performed with the S^{6+} fraction in the liquid as either 30% (hachured region) or 20% (blue region, our preferred value), which then degasses as an SO_2–H_2S mix (we calculate degassing trajectories for SO_2/H_2S ratios between 1 and 10). Our preferred estimate of SO_2/H_2S in the gas, consistent with the measured fO_2 of Reykjanes Ridge basalts, is 5, with these degassing paths shown as solid black ($S^{6+}/\sum S = 0.3$) and blue lines ($S^{6+}/\sum S = 0.2$). In all cases investigated, degassing reduces the basalts, lowering $Fe^{3+}/\sum Fe$. (C) Degassing and fractionation-corrected ferric iron proportions ($[Fe^{3+}/\sum Fe]_{(g,10)}$) after applying the full Gaillard et al. (2011) degassing model to the samples erupted in less than 500 m water depth, plotted as a function of distance from the Iceland plume. For these samples the original ferric iron proportions (grey symbols) have been recalculated back to a water depth of 500 m (coloured symbols joined to grey symbols), largely removing the effect of S degassing.

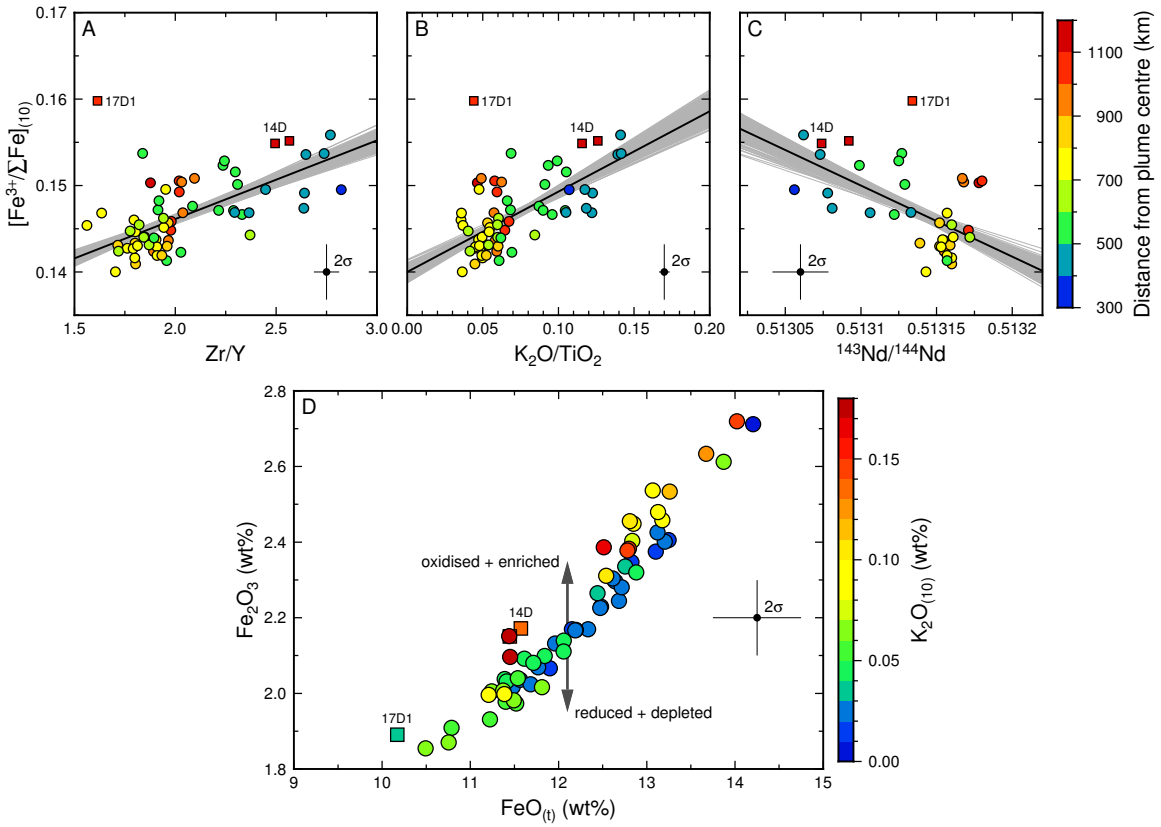

Figure 8: Correlation between oxidation and geochemical indices of enrichment, Zr/Y (A), K_2O/TiO_2 (B), $^{143}Nd/^{144}Nd$ (C). Black lines represent weighted regressions through the data (York, 1969), and grey lines simulations where the data has been randomly permuted according to its analytical uncertainty, indicating the stability of the regression result. Correlations between $[Fe^{3+}/\sum Fe]_{(10)}$ and tracers of incompatible element enrichment are significant at the 95% level. In (D) the relatively greater oxidation of the most enriched samples is shown in Fe_2O_3–$FeO_{(t)}$ space, colouring the symbols by their fractionation corrected potassium content ($K_2O_{(10)}$). At a given FeO, samples with higher $K_2O_{(10)}$ tend to have a higher Fe_2O_3. 17D1 is excluded from this analysis because of its non-Iceland plume affinity (Murton et al., 2002). Trace element and isotope data from Murton et al. (2002); Thirlwall et al. (2004); Hilton et al. (2000).

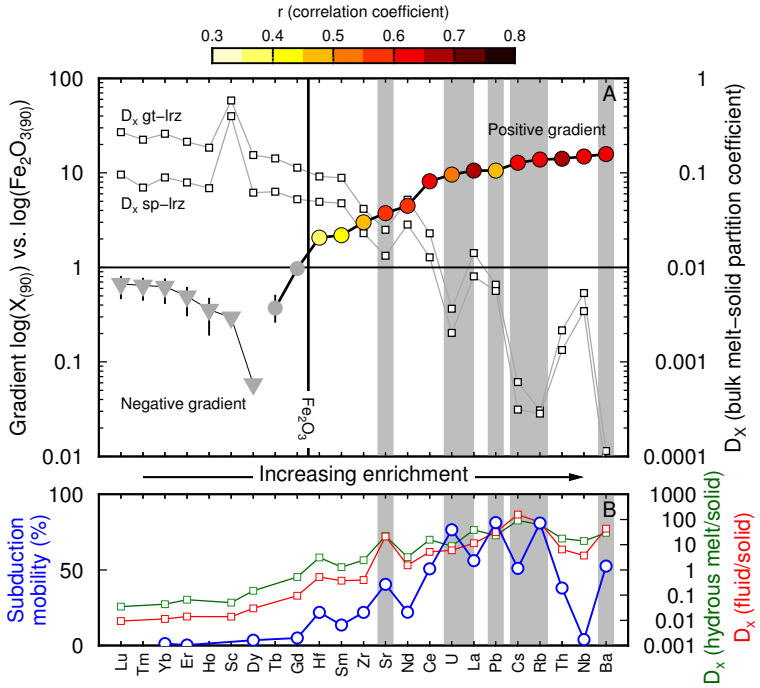

Figure 9: The apparent relative compatibility of trace elements in our sample set relative to Fe_2O_3 (Sims and DePaolo, 1997; Hémond et al., 2006). (A) Trace element data corrected for fractional crystallisation to Fo_{90} have been plotted against Fe_2O_3 in a log–log plot and the gradient and correlation coefficient calculated. Circles record positive gradients and triangles negative gradients (absolute values plotted); coloured symbols have correlations significant at $> 95\%$ confidence level, and error bars are 95% confidence bounds on the calculated gradients. A gradient of unity in log(trace element) vs. $\log(Fe_2O_3)$ space indicates similar compatibility between the two elements considered, placing the effective compatibility of Fe_2O_3 close to Gd. Square symbols record the bulk garnet lherzolite– and spinel lherzolite–melt partition coefficients (Gibson and Geist, 2010), implying $D_{Fe_2O_3} \sim 0.1$. Elements exhibiting under-enrichment with respect to their silicate–melt partition coefficients are highlighted in grey. (B) The mobility of trace elements during subduction from Stracke et al. (2003a) (circles) and the experimentally determined hydrous melt–solid and fluid–solid partition coefficients of Kessel et al. (2005). Trace elements exhibiting relative under-enrichment compared to that predicted by their silicate–melt partition coefficients systematically exhibit higher fluid-mobility during subduction zone processing.

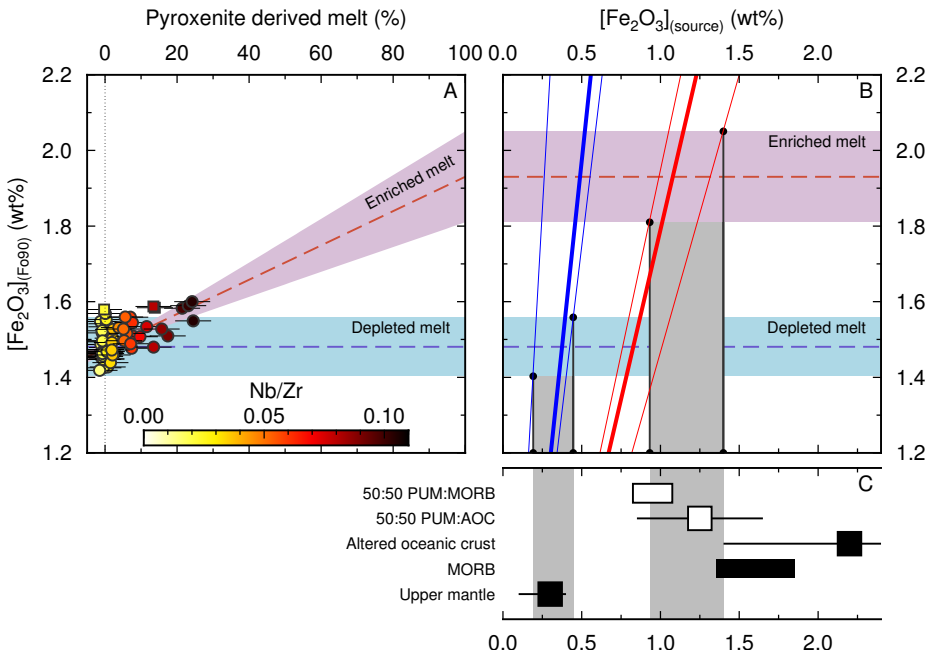

Figure 10: Determining the Fe_2O_3 concentration of the enriched Icelandic plume component. (A) The proportion of recycled pyroxenite melt contributing to basalt compositions is estimated using the method of Shorttle et al. (2014). This estimate is regressed (dashed line with 95% confidence interval) against the fractionation-corrected $[Fe_2O_3]_{(Fo90)}$ to determine the $[Fe_2O_3]_{(Fo90)}$ for a pure melt of the enriched endmember. (B) A simple accumulated fractional melting model is used to relate the inferred primary magmatic $[Fe_2O_3]_{(Fo90)}$ for the depleted (dashed blue line with 95% confidence envelope) and enriched (dashed red line) to that in the source, $[Fe_2O_3]_{(source)}$. Solid thick blue line represents the locus of aggregate melts for a range of source compositions using partition coefficients calculated for a spinel lherzolite (Mallmann and O'Neill, 2009). Thin lines represent how this locus of source composition changes taking endmember cases of melt fraction and partition coefficient values (F = 7–13% and $D_{Fe_2O_3}$ = 0.1–0.23 respectively). Red lines use partition coefficients and melt fractions appropriate to the more fusible garnet-rich pyroxenite lithology inferred to comprise the enriched Icelandic source component (Shorttle and Maclennan, 2011) (F = 15–21% and $D_{Fe_2O_3}$ = 0.47–0.64). Vertical grey bars mark the source compositions which, given the assumptions regarding F and $D_{Fe_2O_3}$, are consistent with the observed melt compositions. (C) Viable source Fe_2O_3 contents are compared to plausible mantle lithologies as black symbols (O'Neill et al., 1993; Lécuyer and Ricard, 1999; Cottrell and Kelley, 2011). White symbols indicate the Fe_2O_3 estimated for the enriched Icelandic source, made of equal proportions of primitive upper mantle (PUM) and either fresh MORB or altered oceanic crust (AOC, (Shorttle and Maclennan, 2011)).

Appendix A. Additional figures and tables

Table A.1: Step sizes and dwell times used for XANES analysis of the Fe K-edge.

Energy range (eV)	Step size (eV)	Dwell time (s)
7020.0–7100.0	10	1
7101.0–7104.0	1.0	2
7104.1–7109.9	0.1	5
7110.0–7117.9	0.1	10
7118.0–7119.4	0.1	5
7119.5–7127.0	0.5	2
7128.0–7144.0	1.0	2
7148.0–7408.0	4.0	2
7410.0–7500.0	10	1

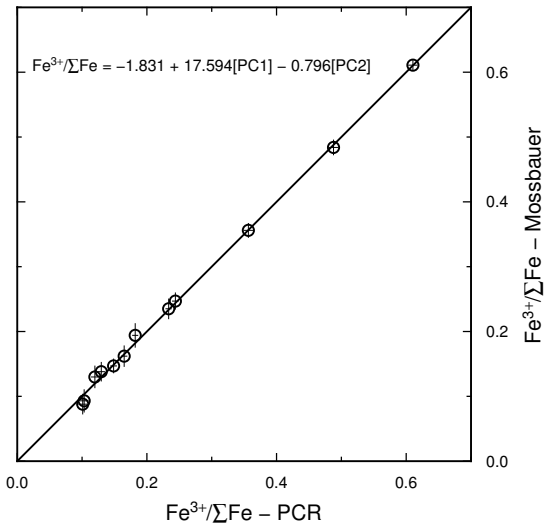

Figure A.1: The result of performing principal component regression (PCR) to take a linear mixture of the first two principal components (Fig. 3) to reconstruct the Mössbauer-derived $Fe^{3+}/\sum Fe$.

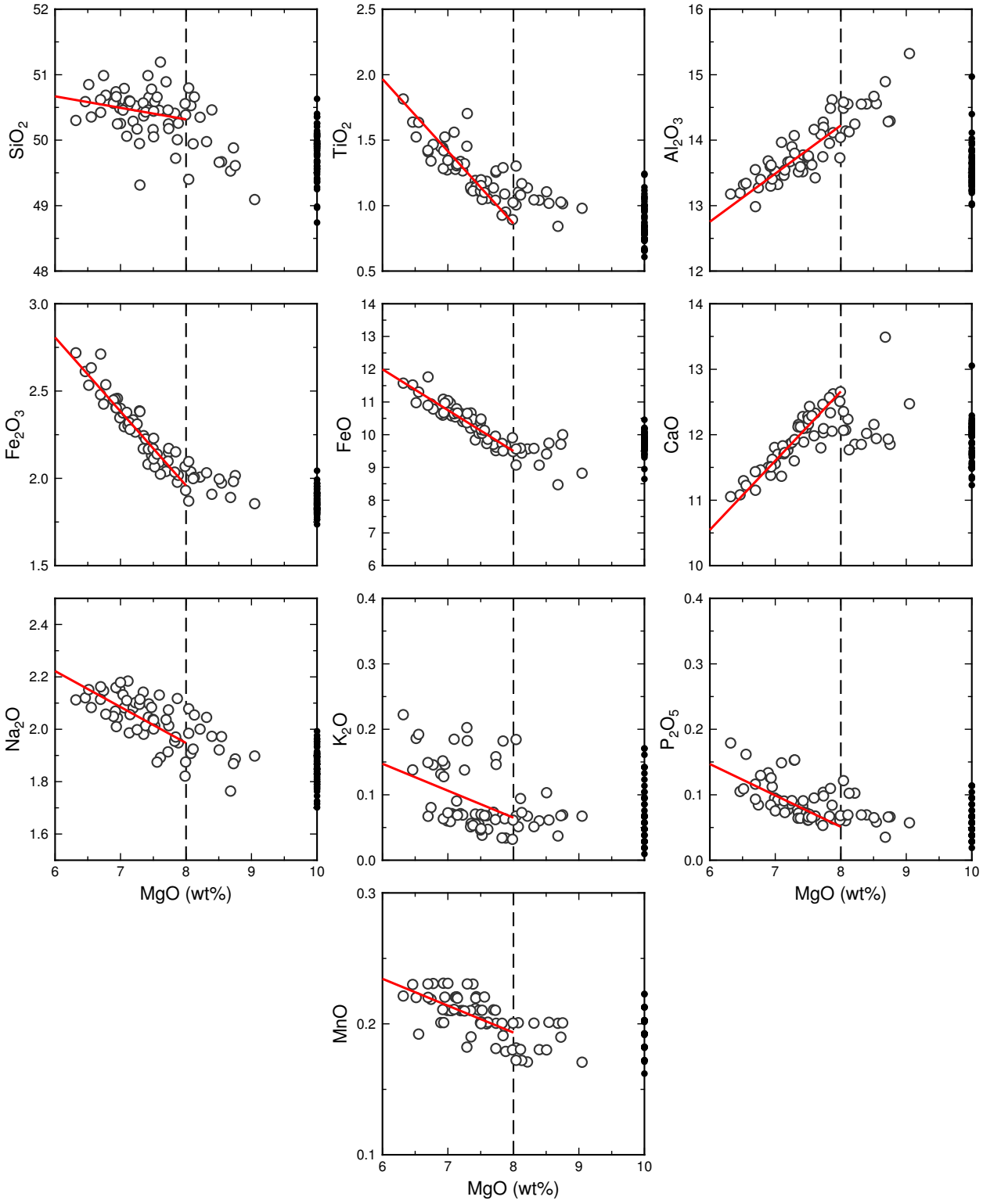

Figure A.2: Plots illustrating how the fractional crystallisation correction has been applied to the data. Samples below 8 wt% MgO first had their MgO content increased to 8 wt%, moving their major element compositions parallel to the red lines in the figures. These lines were calculated by York (1969)-style regression through all the data with MgO < 8 wt%. Subsequent correction to 10 wt% MgO, or Fo_{90}, occured via olivine addition using the Herzberg and O'Hara (2002) olivine model.

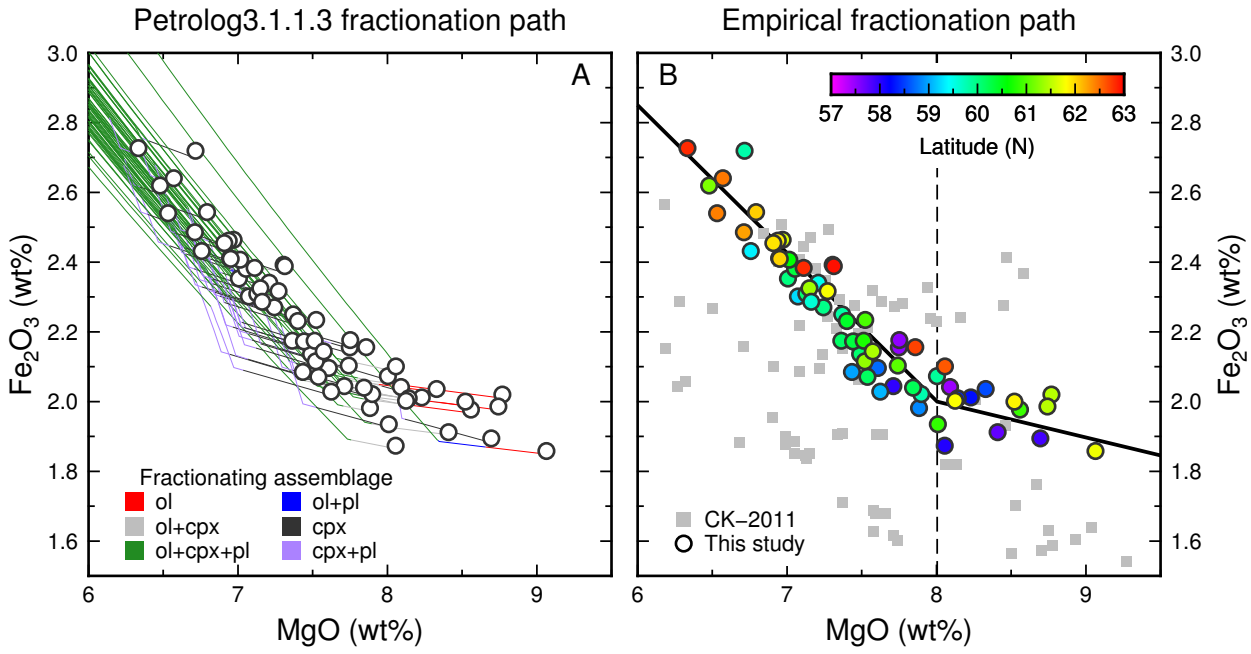

Figure A.3: A comparison between models of fractionation in the Reykjanes Ridge dataset and empirical fits to the data. In (A) Petrolog (version 3.1.1.3, Danyushevsky and Plechov (2011)) is used to model fractional crystallisation starting from the major element composition of the sample glasses (open circles) and using the water data of Nichols et al. (2002). Pressure is set to 2 kbar, partition coefficients are $D_{ol}^{Fe_2O_3} = 0$, $D_{plag}^{Fe_2O_3} = 0$ and $D_{cpx}^{Fe_2O_3} = 0.45$ (Mallmann and O'Neill, 2009), and we used the mineral-melt models of Herzberg and O'Hara (2002). Fractionation paths are drawn as coloured lines showing the co-crystallising phases. (B) shows the mixed empirical (for samples with MgO < 8 wt%) and model (olivine addition to samples above 8 wt% MgO) method of data correction that has been used to construct figures in the main text. Coloured circles are the new data we present here; grey squares are data from Cottrell and Kelley (2011).

Table A.2: Covariance and correlation matrices for parameters in the PCR calibration: $Fe^{3+}/\sum Fe = a_0 + a_1PC1 + a_2PC2$.

	Correlation matrix			Covariance matrix		
	a_0	a_1	a_2	a_0	a_1	a_2
a_0	1.000	-0.999	-0.054	0.009	-0.08	-0.002
a_1	-0.999	1.000	0.0531	-0.08	0.7	0.02
a_2	-0.054	0.0531	1.000	-0.002	0.02	0.2

Table A.3: Calculated bulk partition coefficients used in modelling for Fig. 10, f is the fraction of each mineral phase in the source, sp = spinel, gt = garnet, ol = olivine, opx = orthopyroxene, cpx = clinopyroxene.

lithology	$f_{sp}D_{sp}$	$f_{gt}D_{gt}$	$f_{ol}D_{ol}$	$f_{opx}D_{opx}$	$f_{cpx}D_{cpx}$	$D_{bulk} = \sum f_i D_i$
Spinel lherzolite	0.044	-	0.034	0.050	0.082	0.21
Spinel pyroxenite	0.154	-	0.011	0.030	0.027	0.47
Garnet pyroxenite	-	0.27–0.41	0.014	-	0.23	0.51–0.65

Table A.4: Bulk partition coefficient and melt fraction combinations used in constructing the upper and lower bounds (thin lines) and preferred solution (thick line) for source Fe_2O_3 shown in Fig. 10. sp − lrz = spinel lherzolite, gt − px = garnet pyroxenite, sp − px = sp pyroxenite.

Source	Bound	Lithology	D_{bulk}	F
Depleted	lower	sp-lrz	0.1	0.07
Depleted	upper	sp-lrz	0.23	0.13
Depleted	preferred	sp-lrz	0.21	0.1
Enriched	lower	sp-px	0.47	0.15
Enriched	upper	gt-px	0.65	0.21
Enriched	preferred	gt-px	0.51	0.18